PCCP

DFT simulation of the X-ray diffraction pattern of the aluminum-ion intercalated graphite used as the cathode material of the aluminum-ion battery

SCHOLARONE™
Manuscripts

DFT simulation of the X-ray diffraction pattern of the aluminum-ion intercalated graphite used as the cathode material of the aluminum-ion battery

Jiang Li[1,2]*, Qinghua Liu[4], Raul Abram Flores[1,2], John Lemmon[4]*, Thomas Bligaard[2,3]*

[1]Department of Chemical Engineering, Stanford University, Stanford, California 94305, United States

[2]SUNCAT Center for Interface Science and Catalysis, SLAC National Accelerator Laboratory, 2575 Sand Hill Road, Menlo Park, California 94025, United States

[3]Department of Energy Conversion and Storage, Technical University of Denmark, DK 4000 Roskilde, Denmark

[4] Center of New Energy, National Institute of Clean-and-Low-Carbon Energy, Future Science Park, Changping District, Beijing 102211, China.

ABSTRACT

Many breakthroughs have been achieved in rechargeable aluminum-ion battery technologies in recent years. Most recently, operando X-ray diffraction (XRD) combined with density functional theory (DFT) calculations was reported to study the chloroaluminate anions ($AlCl_4^-$) intercalated graphite cathode of the battery. However, there are quite a few discrepancies between the measured and simulated XRD patterns. This work is focused on the simulation of XRD patterns of graphite intercalation compounds (GICs) with DFT calculations. Our results reveal that both the geometry of $AlCl_4^-$ in graphite and the gallery height of GICs are dependent on the intercalant density. At the low intercalant density, the gallery height keeps constant, but at high intercalant densities, the gallery height is linearly related to the intercalant density. Our simulated XRD patterns are highly consistent with the measured operando XRD patterns. Not only the angles of the peaks match very well, but also the relative intensities and the corresponding electrode capacities show reasonable agreement with the experimental results. The DFT simulation of the XRD pattern provides significant information on the stage index and the charge capacity of the GIC electrode.

KEYWORDS: DFT Simulation, Operando XRD, Graphite Intercalation Compound, Aluminum-ion Battery

1. Introduction

Aluminum-ion battery technology has been considered a promising energy storage device for applications in both portable electronics and stationary applications, owing to its potential advantages over lithium-ion batteries in natural resource usage, manufacturing cost, volumetric capacity, reliability, and safety.[1-7] This is especially encouraged by the breakthrough made by Lin *et al.*[8] who developed a high-performance aluminum-ion battery with an aluminum (Al) foil anode, ionic liquid as the electrolyte, and graphitic foam as the cathode. The battery exhibited ultrafast charging/discharging capability, excellent cycling stability, and high discharge voltage. It is believed that the outstanding performance of the Al/graphite battery is greatly benefited by utilizing the graphitic foam cathode that allows the chloroaluminate anion ($AlCl_4^-$) to intercalate and deintercalate reversibly between the graphite layers.

Plenty of theoretical studies based on density functional theory (DFT) calculations have been carried out to clarify the fundamentals in the high-performance graphite cathode of the aluminum-ion battery.[9-13] After Lin *et al.*[8] reported their high-performance battery, Wu *et al.*[11] simulated $AlCl_4^-$ intercalated in graphite and found that $AlCl_4^-$ was in planar quadrangle geometry in graphite and the ultrafast charging/discharging capability of the battery was due to the extremely low diffusion barrier (0.023 eV) of $AlCl_4^-$ in the graphite bulk. However, later DFT studies consistently concluded that the intercalated $AlCl_4^-$ in graphite was in a tetrahedron geometry rather than in a planar quadrangle.[9-10, 12-13] Jung *et*

al.[9] concluded that $AlCl_4^-$ was stored in a doubly stacked tetrahedron in the interlayer. They attributed the ultrafast rate capability of the graphite cathode to its nanoscale thickness, according to their simulated results that demonstrated the diffusivity of $AlCl_4^-$ in a graphite film was two orders of magnitude larger than in the bulk graphite. Bhauriyal *et al.*[10] investigated the staging mechanism of $AlCl_4^-$ intercalation into graphite and found that the initial intercalation step was more sluggish than subsequent intercalation steps and the process preferred to extend in the same interlayer, until $AlCl_4^-$ reaches the maximum occupancy, before migrating to deeper layers. Gao *et al.*[12] systematically studied $AlCl_4^-$ intercalated graphite by investigating intercalant geometry, graphite stacking, stage and gallery height, simulation of the charging potential profile, and diffusion of $AlCl_4^-$ in bulk graphite. They provided a comprehensive understanding of the graphite cathode of the aluminum-ion battery. One of the most impressive conclusions drawn by Gao *et al.*[12] is that the diffusion barrier of $AlCl_4^-$ was in the range of 0.012 to 0.029 eV, much smaller than the barrier for lithium-ion diffusion in graphite (~ 0.2 eV).

Most recently, Pan *et al.*[14] reported an operando X-ray diffraction (XRD) study on the $AlCl_4^-$ intercalated graphite cathode of the aluminum-ion battery. They observed that the discharge capability of the battery at low temperature (-10 °C) was superior to that at room temperature. DFT calculations were also performed in their work to simulate the measured in-situ XRD patterns. Nevertheless, there were few discrepancies between the simulated and measured XRD data, including a ~10% error between the simulated and experimental

peaks at small angles and inconsistent relative peak intensities.

With the increasing application of operando XRD techniques for the study of graphite intercalation compounds (GICs), it is necessary that the DFT simulated XRD patterns be consistent with the experimental results with respects to peak position, peak intensity, and even the corresponding charge capacity of the graphite electrode. In the present work, we employ DFT calculations to study the $AlCl_4^-$ intercalated graphite. We concentrate on simulating XRD patterns of graphite cathodes during the whole charging process of the Al/graphite battery. Our simulated results are compared with the most recently reported operando XRD patterns of $AlCl_4^-$-GIC.[14] Moreover, the debate concerning the geometry of $AlCl_4^-$ in graphite is investigated. The gallery heights of the $AlCl_4^-$-GIC at different intercalation stages and with varying intercalant densities are examined and discussed.

2. Computational method

DFT calculations were carried out using the Quantum Espresso software package interfaced with the Atomic Simulation Environment (ASE).[15-16] The BEEF-vdW functional was used to describe the exchange and correlation effects and to include van der Waals interactions, which is important to include in graphitic systems.[11, 17] The interactions between the ion cores and the electrons were described with the ultrasoft Vanderbilt pseudopotentials.[18] Plane wave basis sets with a kinetic energy cutoff of 500 eV were used. The Brillouin-zone was sampled with a Monkhorst-Pack grid of $10\times10\times4$ for the graphite

unit cell and a grid of 2×2×2 for the 6×6×1 supercell. The convergence criterion for the

self-consistent-field calculation was set to 10^{-5} eV. Structure optimization was performed

by fully relaxing both the atomic positions and the lattice parameters until the forces on all

the atoms were within 0.03 eV/Å. During our DFT simulation, we treated the

chloroaluminate anion ($AlCl_4^-$) in graphite as a charge-neutral species as did by other

colleagues[12].

3. Results and discussion

3.1 Geometry of $AlCl_4^-$ in graphite

Graphite is known to have an AB stacking pattern where the vertices of the carbon

hexagon in the A layer are above the center of the carbon hexagon in the B layer and

theoretical studies have shown that this remains the case when $AlCl_4^-$ is intercalated

between the sheets.[10, 12] Similar stacking is also experimentally observed both in pristine

and $FeCl_3$ intercalated graphite.[19] All the graphite models in the present work are built with

AB stacking.

Recent DFT studies have shown that the intercalated $AlCl_4^-$ in graphite is in

tetrahedron geometry.[9-10, 12] However, the tetrahedron $AlCl_4^-$ can either in a lying position

with the two Cl atoms pointing up and the other two pointing down or in a standing position

with one Cl atom directed out of the plane and the other three sitting in the same plane, as

shown in Figure 1a and 1b, respectively.
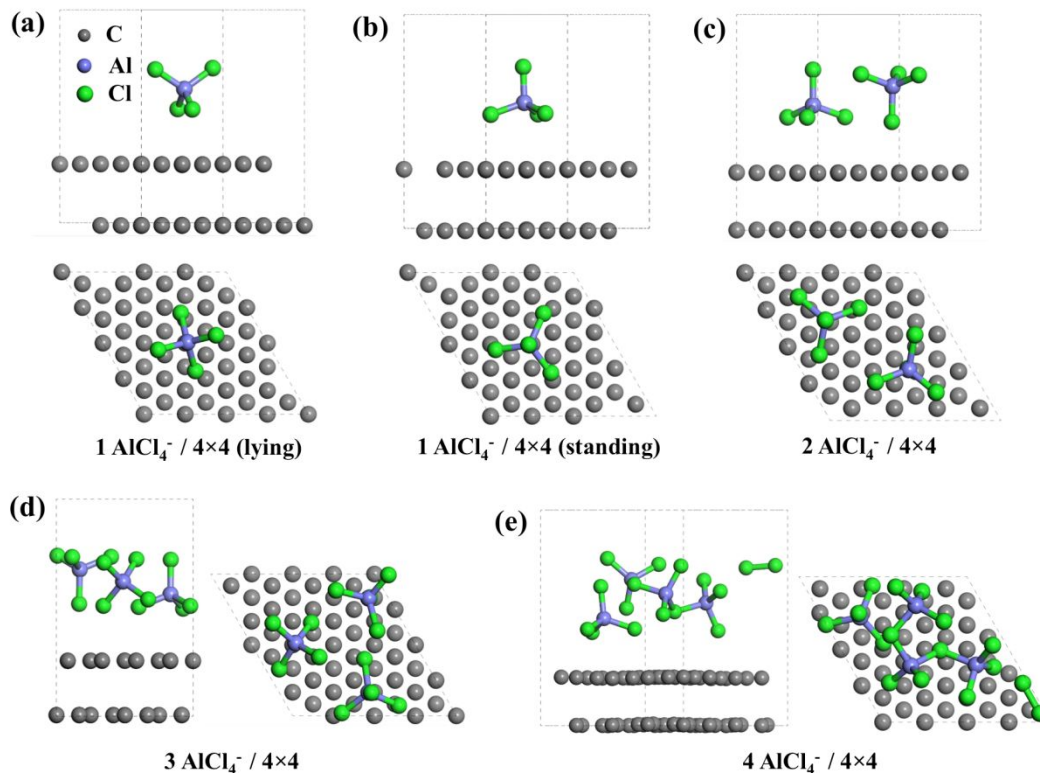
Figure 1. Stable configurations of $AlCl_4^-$ in graphite at different intercalant densities. The graphite supercell is composed of $4\times4\times1$ graphite unit cells. (a) One $AlCl_4^-$ in the supercell, with a lying configuration. (b) One $AlCl_4^-$ in the supercell, with a standing configuration. (c) Two $AlCl_4^-$ in the supercell, both of these two $AlCl_4^-$ are with standing configurations, one pointing up and the other pointing down. (d) Three $AlCl_4^-$ in the supercell, with one lying, one heading down, and one heading up (e) Four $AlCl_4^-$ in the supercell, the $AlCl_4^-$ tetrahedrons connect each other and release the excess Cl atoms in the form of chlorine.

For one $AlCl_4^-$ in the $4\times4\times1$ graphite supercell, denoted as $1AlCl_4^-/4\times4$, the lying position (Figure 1a) is 0.11 eV more stable than the standing position (Figure 1b), consistent with the reported[12] result that the energy of the lying configuration is 0.08 eV lower than that of the standing one. However, for the $2AlCl_4^-/4\times4$ graphite (Figure 1c), it

is stabilized by two standing $AlCl_4^-$ with one heading up and the other heading down. This agrees with the result obtained by Jung *et al.*[9]. Interestingly, for the $3AlCl_4^-/4\times4$ graphite (Figure 1d), the most stable configuration is with one $AlCl_4^-$ heading up, one heading down, and one lying. When the number of the intercalated $AlCl_4^-$ increases to four (Figure 1e), the intercalated $AlCl_4^-$ may connect with each other, sharing some Cl atoms and spontaneously releasing the excess Cl atoms in the form of chlorine. Therefore, the geometry of $AlCl_4^-$ in graphite is dependent on the intercalant density. At low densities, the lying configuration is energetically favorable, while at high densities, the lying and standing configurations connect with each other to stabilize the whole intercalant layer.

3.2 Stage and gallery height

The staging phenomenon is the most important ordering property of GICs, characterized by the period arrangement of the intercalant layers in the matrix of the host graphite layers. Stages of GICs are classified by a stage index *n* representing the number of graphite layers between two adjacent intercalant layers.[19] The stage-*n* GICs are modeled by 2×2, 3×3, and 4×4 graphite unit cell on the *ab* plane and *n* graphene layers along the *c* direction, as shown in Figure 2a, 2b, and 2c, respectively.
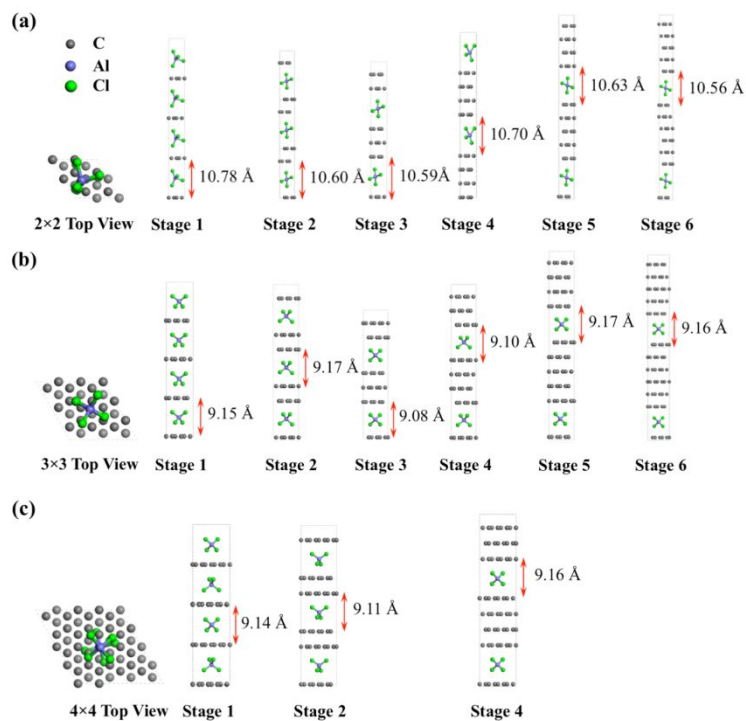
Figure 2. Gallery heights of intercalated graphite at different stages and intercalant densities. (a) Gallery heights of graphite for all stages, at intercalant density of $1AlCl_4^-$/2×2. (b) Gallery heights of graphite for all stages, at intercalant density of $1AlCl_4^-$/3×3. (c) Gallery heights of graphite for stages 1, 2 and 4, at intercalant density of $1AlCl_4^-$/4×4.

Evidently, the intercalant gallery height (d_i), *i.e.*, the distance between the two adjacent graphene layers that are above and below the intercalant layer, is almost independent of the stage index n but has an appreciable dependence on the intercalant density. At a small intercalant density of $1AlCl_4^-$/4×4, d_i is nearly the same with that at the density of $1AlCl_4^-$/3×3. Nevertheless, with the intercalant density increasing from $1AlCl_4^-$/3×3 to $1AlCl_4^-$/2×2, d_i increases from ~9.14 to ~10.60 Å. Therefore, at low intercalant density, d_i is approximately a constant, but at high intercalant density, the effect of intercalant density on d_i cannot be ignored. Bhauriyal *et al.*[10] pointed out that d_i is a constant

for all the stages with varying intercalant densities, but the highest intercalant density they

modeled is $4AlCl_4^-/6\times6$, which has the same density as the $1AlCl_4^-/3\times3$ system modeled in

the present work.
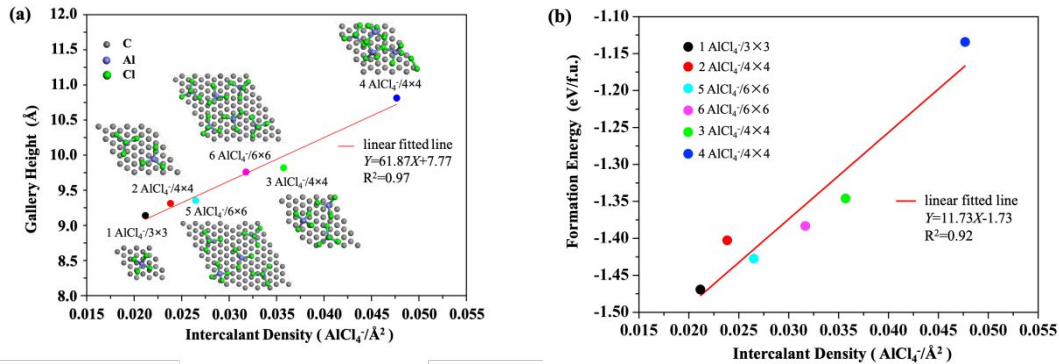
Figure 3. (a) Linear relationship between the gallery height and the intercalant density.

The value of the intercalant density is defined as the number of $AlCl_4^-$ divided by the area

of the graphite supercell on the *ab* plane. (b) Linear relationship between the formation

energy of $AlCl_4^-$-GIC and the intercalant density. The unit of the formation energy is eV

per formula unit (f.u.) of $AlCl_4^-$.

Since the stage of GIC has no effect on the gallery height, we choose the stage-2 GICs

to further investigate the effect of intercalant density on the gallery height. 3×3, 4×4, and

6×6 repetitions of the graphite unit cell on the *ab* plane are constructed for the stage-2

GICs. Varying number of $AlCl_4^-$ tetrahedrons are placed in the intercalant layer to model

different intercalant densities. The result is shown in Figure 3(a). The area of the graphite

unit cell on the *ab* plane is $2.461^2\times\sqrt{3}/2=5.24$ Å^2. The intercalant density is defined as the

number of $AlCl_4^-$ ions divided by the area of the graphite supercell in the *ab* plane. When

the intercalant density is larger than 0.021 $AlCl_4^-/$Å^2, which corresponds to $1AlCl_4^-/3\times3$,

the gallery height of the GIC is linearly related to the intercalant density, with R^2 as high

as 0.97. As mentioned above, the upper limit occupancy of the intercalant layer is $4AlCl_4^-$

$/4\times4$ (0.048 $AlCl_4^-/Å^2$). When the intercalant density is smaller than 0.021 $AlCl_4^-/Å^2$, the

gallery height can be regarded as a constant. The energetics of the intercalated GICs with

different intercalant densities can be expressed with the formation energy (E_f) defined as

follows,

$$E_f = [E(xAlCl_4^--GIC) - xE(AlCl_4^-) - E(G)]/x \qquad (1)$$

where $E(xAlCl_4^--GIC)$ denotes the energy of the $AlCl_4^-$ intercalated GIC, x is the number

of $AlCl_4^-$ that intercalated in the GIC, $E(AlCl_4^-)$ is the energy of $AlCl_4^-$, and $E(G)$ is the

energy of pristine graphite. Formation energies of the intercalated GICs with different

intercalant densities are shown in Figure 3(b). It turns out that the formation energy of

$AlCl_4^--GIC$ is almost linearly related to the intercalant density, with R^2 being 0.92. With

the intercalant density increasing from $1AlCl_4^-/3\times3$ (0.021 $AlCl_4^-/Å^2$) to $4AlCl_4^-/4\times4$

(0.048 $AlCl_4^-/Å^2$), the formation energy increases by 0.34 eV from -1.47 to -1.13 eV, which

is due to the increasing repulsion reaction between the intercalated $AlCl_4^-$ tetrahedrons at

augmented intercalant density. The formation energy defined in eq. (1) is   slightly

different from that defined by Gao et $al.$[12] In our case, the unit of the formation energy is

eV per formula unit (f.u.) of $AlCl_4^-$. If we plot the total formation energy with the number

x of $AlCl_4^-$ intercalated in the graphite, the total formation energy will linearly decrease

with increasing x, which has the same trend with that in Gao's work[12].

It should be noted that our calculated distance between the two graphene layers of the pristine graphite is 3.51 Å, slightly larger than the experimental value of 3.35 Å, and our calculated height of the empty gallery of GICs is also about 3.51 Å for all stages with different intercalant densities. In the present work, the DFT derived gallery height of GICs is overestimated by a factor of 3.51/3.35=1.05. Therefore, the directly calculated gallery height needs to be divided by a correction factor (1.05) to be comparable with the experimental results. After corrected, the final simulated gallery heights d_i of $AlCl_4^-$-GIC at low intercalant density (< 0.021 $AlCl_4^-/Å^2$) ranges from 8.65 to 8.73 Å, which is highly consistent with the simulated value of 8.36~8.76 Å reported by Bhauriyal et al.[10]. In the following simulation of the XRD pattern, the height of empty gallery (d_0) of GIC is based on the experimental value (3.35 Å) and the gallery height d_i is adjusted with the correction factor (1.05).

3.3 XRD simulation

The diffraction angle (θ_l) of the (00l) peak on the XRD pattern can be simulated according to the Bragg's law,[19]

$$l\lambda = 2I_c\sin\theta_l \qquad (2)$$

where λ is the X-ray wavelength of 1.54 Å, I_c is the periodic repeat distance along the stacking direction. For the stage-n GIC, I_c is expressed as

$$I_c = d_i + (n\text{-}1)\, d_0 = d_i + (n\text{-}1) \times 3.35 \qquad (3)$$

As mentioned above, at high intercalant density (> 0.021 $AlCl_4^-/Å^2$), the gallery height

d_i is linearly related to the intercalant density (D_i), *i.e.*,

$$d_i = (A \cdot D_i + B)/1.05 \qquad (4)$$

where A and B are the simulated slope (61.87) and intercept (7.77), respectively. The denominator 1.05 is the correction factor, adjusting for the difference between the DFT calculated and experimental gallery heights.

Experimentally, the charge capacity (C_i) of an electrode is measurable, and can be expressed in terms of the intercalant density D_i,[14]

$$C_i = \frac{D_i \cdot S_C \cdot F}{3.6 \cdot (n \cdot N_C) \cdot M_C} \qquad (5)$$

where S_C is the area of the graphite unit cell on the *ab* plane, which is computed to be 5.24 Å^2, F is the Faraday constant of 96485 C/mol. N_C is the number of carbon atoms in a single layer of the graphite unit cell, *i.e.*, $N_C = 2$. M_C is the molar mass of carbon atom, *i.e.*, $M_C = 12$ g/mol. The factor of 3.6 in the denominator ensures the unit of C_i to be mAh/g.

According to eqs. (2)-(5), the diffraction angle on the XRD pattern can be simulated and related to the capacity of the graphite electrode.

In addition, the intensity of the (00l) reflection is proportional to the square of the structure factor ($|F_{00l}|^2$). For a GIC, F_{00l} is expressed as,[20]

$$F_{00l} = \xi f_i + (-1)^l f_C \frac{sin(n\pi x l)}{sin(\pi x l)} \qquad (6)$$

where ξ is the molar ratio of the intercalant atoms to the carbon atoms. f_i and f_C are the scattering factors for the intercalant atoms and the carbon atoms, respectively, which are given in the crystallography handbook.[21] The variable x is equal to $d_0/I_c = 3.35/I_c$. Usually,

the number of intercalant atoms is much smaller than the carbon atoms in the graphite

matrix, so that the contribution from f_i can be neglected and the relative intensity of the

(00l) reflection (η_l) can be simply calculated with the following equation,

$$\eta_l = f_C^2 \frac{sin^2(n\pi xl)}{sin^2(\pi xl)} \tag{7}$$

The simulated XRD patterns of the AlCl$_4^-$-GIC for all stages at varying charge

capacities are shown in Figure 4.
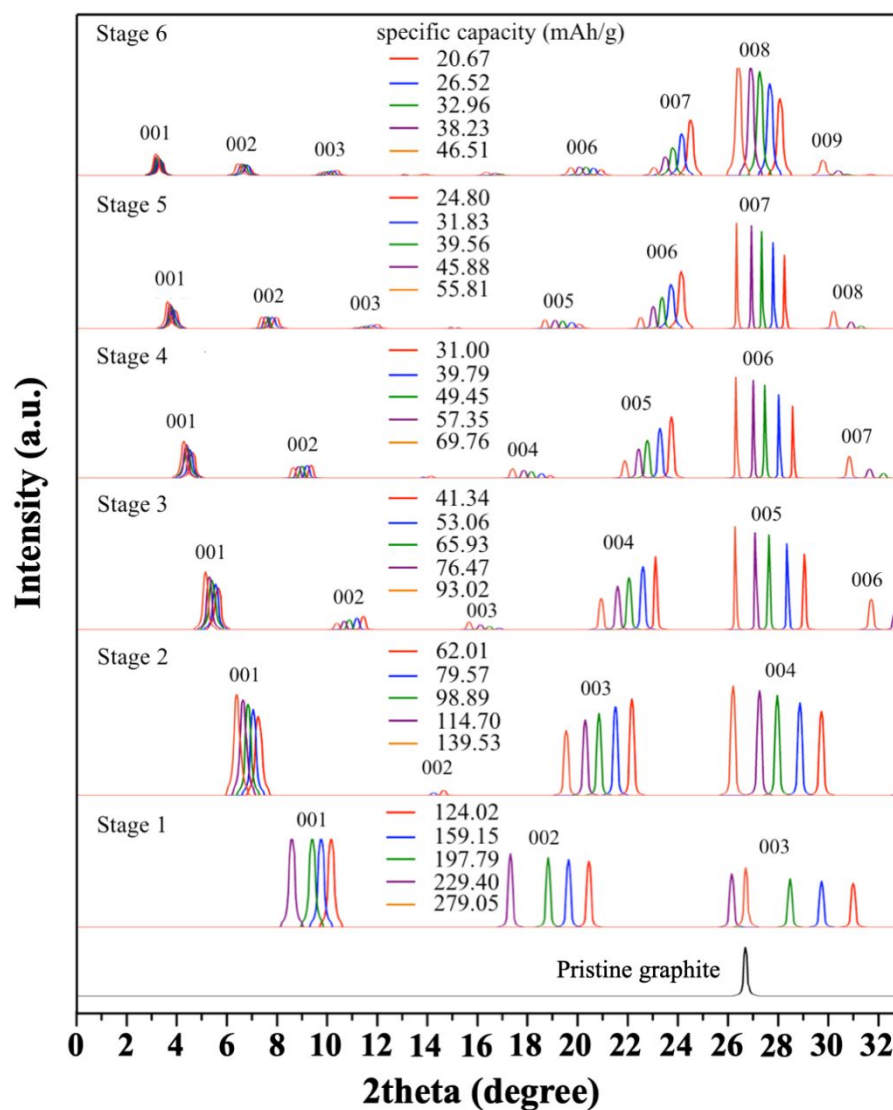
Figure 4. Simulated XRD patterns of the AlCl$_4^-$-GIC for stages 1 to 6 at varying charge

capacities. For each stage, only five different charge capacities are shown. A peak index

(00l) is shown on the top of the corresponding peaks.

As the stage index n decreases from 6 to 1, the peaks with the same (00l) index shift

rightward. At a fixed stage-n, the increasing charge capacity makes the peaks shift leftward,

with peaks at large angles shifting more than those at small angles. For instance, with a

capacity increase from 20.67 to 46.51 mAh/g, the (008) peak of the stage-6 GIC shifts from

28.02 to 26.36 degree, while the (001) peak shifts by only 0.2 degrees (from 3.47 to 3.27

degrees). The peaks at small angles are minimally affected by the capacity of the graphite

electrode, making them more reliable experimental indicators of the stage index under

operating conditions. At each stage, five capacities are shown in Figure 4, including the

lower and upper limits of the capacity, and three additional intermediate capacities. The

lower limit capacity corresponds to the intercalant density of 0.021 $AlCl_4^-/Å^2$, below which

the gallery height of the intercalant layer remains constant. The upper limit capacity

corresponds to the maximum occupancy of the intercalant layers with a density of 0.048

$AlCl_4^-/Å^2$, above which the intercalated $AlCl_4^-$ may interact with each other releasing

chorine molecules. If the capacity of the stage-n GIC is smaller than the lower limit, the

XRD pattern will be the same with the pattern at the lower limit because the gallery height

of the GIC is a constant at low intercalant densities. If the capacities are larger than the

upper limit, the XRD pattern will continue to shift to lower theta values, but at these

capacities the $AlCl_4^-$ ions will interact strongly and form chlorine gas, which process may

result in severe charge capacity loss and   induce deleterious expansion of the graphite

structure. The maximum peak intensity appears at $(00l_M)$ where $l_M = n + 2$, which is

consistent with the experimental finding that $l_M = n + m_i$ where m_i is the nearest integer to

the ratio $(d_i - d_0)/d_0 = 5.35/3.35 \approx 2$.[19] In addition, the intensities of the $(00l)$ peaks at stage-

n with l equal to n, n-1, n-2, …, and n-m (n-m>2) are low enough to be negligible.

The simulated XRD patterns of $AlCl_4^-$-GIC with stage-6 at 32.96 mAh/g, stage-5 at

39.56 mAh/g, stage-4 at 49.45 mAh/g, and stage-3 at 65.93 mAh/g are shown in Figure 5.

The simulated XRD patterns agree well with the operando XRD patterns measured by Pan

et $al.$[14], with respects to the diffraction angles, peak intensities, and charge capacities.
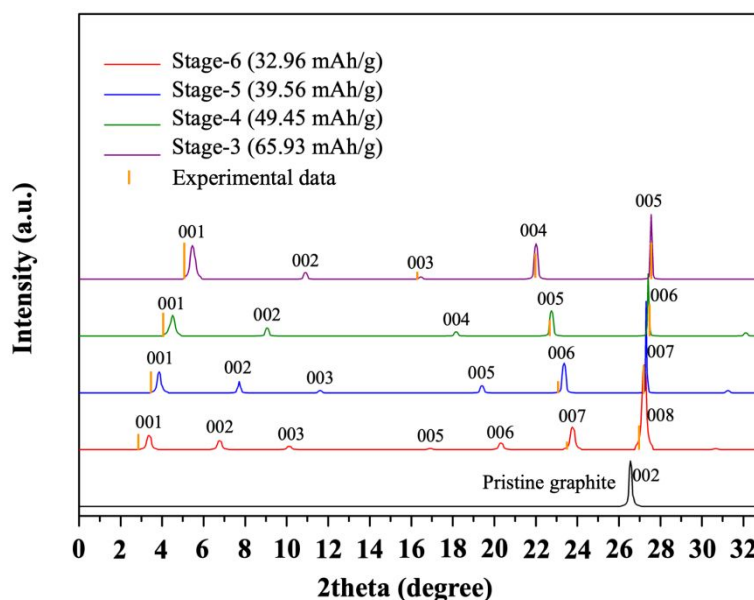
Figure 5. Simulated XRD patterns the $AlCl_4^-$-GIC with stage index ranging from 6 to 1 at

certain charge capacity. The orange solid line represents the experimental data reported by

Pan et $al.$[14]

The simulated angles of the (001) peaks at stage-n (n = 6, 5, 4, 3) are respectively 3.4,

3.9, 4.5, and 5.4 degrees, which are slightly larger than the experimental results with the corresponding values of 2.9, 3.5, 4.1, and 5.1 degrees. At the $(00l_M)$ $(l_M = n + 2)$ and $(00l_{NM})$ $(l_{NM} = n + 1)$ peaks, the simulated angles are in good agreement with experimental ones with the maximum difference smaller than 0.2 degree. What's more, the experimentally determined (003) peak of stage-3 appears at 16.3 degrees, which compares well with our simulated result of 16.4 degrees.

In terms of the relative intensities of the peaks, both the simulated and the experimental results show that the $(00l_M)$ peak exhibits the highest intensity. Experimentally, only the (001), $(00l_{NM})$, and $(00l_M)$ peaks are clearly visible; in the theoretical simulation, these three peaks have the largest intensities. With the stage index n decreasing from 6 to 3, the simulated intensities of the (001) and $((00l_{NM})$ peaks relative to the $(00l_M)$ peak increase gradually, which is also observed in the measured operando XRD pattern.

Lastly, the charge capacities of the GIC models are reasonably consistent with the experimental values. At stage-3 and stage-4, the modeled specific capacities of the GICs are respectively 65.93 and 49.45 mAh/g, and the corresponding experimental values are about 68 and 48 mAh/g. However, at stage-5 and stage-6, the modeled specific capacities of the GICs are respectively 39.56, and 32.96 mAh/g, which are much larger than the corresponding experimental values, i.e., 17 and 1 mAh/g. This discrepancy is probably due to the experimental underestimation of the electrode capacity during the early charging

process. At the beginning of the charging process, once the galleries between the graphite layers are expanded by the intercalated $AlCl_4^-$, large amount of $AlCl_4^-$ may intercalate into the opened galleries by concentration gradient (diffusion) instead of by electric field (electrochemical migration), making the practical amount of the intercalated $AlCl_4^-$ much larger than the value only calculated according to the charging current.

4. Conclusions

The geometry of $AlCl_4^-$ in graphite and the gallery height of the GIC have been investigated with first principles calculations. The XRD patterns of the GIC for all stages at varying charge capacities have been simulated and compared with the experimental operando XRD patterns. The results reveal that the stable geometry of the $AlCl_4^-$ in graphite highly depends on the intercalant density. At low densities, the lying $AlCl_4^-$ tetrahedron is the most energetically favorable configuration; however, at high densities, multiple configurations of the $AlCl_4^-$ tetrahedrons coordinate with each other to stabilize the whole intercalant layer. The gallery height of the GIC is also dependent on the intercalant density. When the intercalant density is smaller than one $AlCl_4^-$ per 3×3 repetition of graphite unit cell on the *ab* plane, the gallery height is almost a constant of 8.7 Å; when larger than this intercalant density, the gallery height has a linear relationship with the intercalant density. The simulated XRD patterns show that both the stage index *n* and the charge capacity of the GIC affect the diffraction angles of the peaks. The decreasing stage index *n* makes the

peaks shift rightward, while the increasing charge capacity makes the peaks shift leftward. The peaks at small angles are hardly influenced by the charge capacity and are therefore very useful in determining the stage index of a GIC. On the simulated XRD pattern, the $(00l_M)$ $(l_M = n + 2)$ peak has the highest intensity, which is consistent with the experimental findings. The simulated XRD patterns are reasonably consistent with the measured operando XRD patterns in many aspects, including the diffraction angles, relative intensities, and the charge capacities. The DFT simulation of the XRD pattern is an important technique to determine the stage of a GIC and analyze the charge capacity of a graphite electrode.

Conflict of interest statement

There are no conflicts to declare.

Acknowledgments

References

(1)   Li, Q.; Bjerrum, N. J. Aluminum as anode for energy storage and conversion: a review. *J. Power Sources* **2002,** *110*, 1-10.

(2)   Jayaprakash, N.; Das, S.; Archer, L. The rechargeable aluminum-ion battery. *Chem. Commun.* **2011,** *47*, 12610-12612.

(3)   Liu, S.; Hu, J.; Yan, N.; Pan, G.; Li, G.; Gao, X. Aluminum storage behavior of anatase TiO2 nanotube arrays in aqueous solution for aluminum ion batteries. *Energy Environ. Sci.* **2012,** *5*, 9743-9746.

(4)   Reed, L. D.; Menke, E. The roles of V2O5 and stainless steel in rechargeable Al–ion batteries. *J. Electrochem. Soc.* **2013,** *160*, A915-A917.

(5)   Wang, W.; Jiang, B.; Xiong, W.; Sun, H.; Lin, Z.; Hu, L.; Tu, J.; Hou, J.; Zhu, H.; Jiao, S. A new cathode material for super-valent battery based on aluminium ion intercalation and deintercalation. *Scientific reports* **2013,** *3*, 3383.

(6)   Sun, H.; Wang, W.; Yu, Z.; Yuan, Y.; Wang, S.; Jiao, S. A new aluminium-ion battery with high voltage, high safety and low cost. *Chem. Commun.* **2015,** *51*, 11892-11895.

(7)   Liu, S.; Pan, G.; Li, G.; Gao, X. Copper hexacyanoferrate nanoparticles as cathode material for aqueous Al-ion batteries. *Journal of Materials Chemistry A* **2015,** *3*, 959-962.

(8)   Lin, M.-C.; Gong, M.; Lu, B.; Wu, Y.; Wang, D.-Y.; Guan, M.; Angell, M.; Chen, C.; Yang, J.; Hwang, B.-J. An ultrafast rechargeable aluminium-ion battery. *Nature* **2015,** *520*, 324.

(9)   Jung, S. C.; Kang, Y.-J.; Yoo, D.-J.; Choi, J. W.; Han, Y.-K. Flexible few-layered graphene for the ultrafast rechargeable aluminum-ion battery. *The Journal of Physical Chemistry C* **2016,** *120*, 13384-13389.

(10)   Bhauriyal; Bhauriyal, P.; Mahata, A.; Pathak, B. The staging mechanism of AlCl4intercalation in a graphite electrode for an aluminium-ion battery. *PCCP (Physical chemistry chemical physics)* **2017,** *19*, 7980-7989.

(11)   Wu, M. S.; Xu, B.; Chen, L. Q.; Ouyang, C. Y. Geometry and fast diffusion of AlCl4 cluster intercalated in graphite. *Electrochim. Acta* **2016,** *195*, 158-165.

(12)   Gao; Gao, Y.; Zhu, C.; Chen, Z.; Lu, G. Understanding Ultrafast Rechargeable Aluminum-Ion Battery from First-Principles. *The Journal of Physical Chemistry C* **2017,** *121*, 7131-7138.

(13)   Jung, S. C.; Kang, Y.-J.; Han, Y.-K. Comments on "Geometry and fast diffusion of AlCl4 cluster intercalated in graphite [Electrochim. Acta 195 (2016) 158–165]". *Electrochim. Acta* **2017,** *223*, 135-136.

(14)   Pan, C.-J.; Yuan, C.; Zhu, G.; Zhang, Q.; Huang, C.-J.; Lin, M.-C.; Angell, M.;

Hwang, B.-J.; Kaghazchi, P.; Dai, H. An operando X-ray diffraction study of chloroaluminate anion-graphite intercalation in aluminum batteries. *PNAS* **2018,** *115*, 5670-5675.

(15)   Giannozzi, P.; Baroni, S.; Bonini, N.; Calandra, M.; Car, R.; Cavazzoni, C.; Ceresoli, D.; Chiarotti, G. L.; Cococcioni, M.; Dabo, I. QUANTUM ESPRESSO: a modular and open-source software project for quantum simulations of materials. *J. Phys.: Condens. Matter* **2009,** *21*, 395502.

(16)   Bahn, S. R.; Jacobsen, K. W. An object-oriented scripting interface to a legacy electronic structure code. *Computing in Science & Engineering* **2002,** *4*, 56-66.

(17)   Wellendorff, J.; Lundgaard, K. T.; Møgelhøj, A.; Petzold, V.; Landis, D. D.; Nørskov, J. K.; Bligaard, T.; Jacobsen, K. W. Density functionals for surface science: Exchange-correlation model development with Bayesian error estimation. *Phys. Rev. B* **2012,** *85*, 235149.

(18)   Vanderbilt, D. Soft self-consistent pseudopotentials in a generalized eigenvalue formalism. *Phys. Rev. B* **1990,** *41*, 7892.

(19)   Dresselhaus, M. S.; Dresselhaus, G. Intercalation compounds of graphite. *Adv. Phys.* **1981,** *30*, 139-326.

(20)   Silva, M. P. d.; Gualberto, G. M. Structural determination of graphite Fe Cl3, Zn Cl2 using (001) X-ray diffraction. *Braz. J. Phys.* **1995,** *25*, 175-180.

(21)   Prince, E.; Wilson, A. J. C. International tables for crystallography. **2004**.